Interactions between the Responses of North American Climate to El Niño–La Niña and to the Secular Warming Trend in the Indian–Western Pacific Oceans

NGAR-CHEUNG LAU, ANTS LEETMAA, AND MARY JO NATH

NOAA/Geophysical Fluid Dynamics Laboratory, Princeton University, Princeton, New Jersey

(Manuscript received 16 February 2007, in final form 30 May 2007)

ABSTRACT

The modulation of El Niño and La Niña responses by the long-term sea surface temperature (SST) warming trend in the Indian–Western Pacific (IWP) Oceans has been investigated using a large suite of sensitivity integrations with an atmospheric general circulation model. These model runs entail the prescription of anomalous SST conditions corresponding to composite El Niño or La Niña episodes, to SST increases associated with secular warming in IWP, and to combinations of IWP warming and El Niño/La Niña. These SST forcings are derived from the output of coupled model experiments for climate settings of the 1951–2000 and 2001–50 epochs. Emphasis is placed on the wintertime responses in 200-mb height and various indicators of surface climate in the North American sector.

The model responses to El Niño and La Niña forcings are in agreement with the observed interannual anomalies associated with warm and cold episodes. The wintertime model responses in North America to IWP warming bear a distinct positive (negative) spatial correlation with the corresponding responses to La Niña (El Niño). Hence, the amplitude of the combined responses to IWP warming and La Niña is notably higher than that to IWP warming and El Niño. The model projections indicate that, as the SST continues to rise in the IWP sector during the twenty-first century, the strength of various meteorological anomalies accompanying La Niña (El Niño) will increase (decrease) with time. The response of the North American climate and the zonal mean circulation to the combined effects of IWP forcing and La Niña (El Niño) is approximately equal to the linear sum of the separate effects of IWP warming and La Niña (El Niño).

The summertime responses to IWP warming bear some similarity to the meteorological anomalies accompanying extended droughts and heat waves over the continental United States.

1. Introduction

El Niño–Southern Oscillation (ENSO) is one of most significant modes of climate variability on interannual time scales. Its impacts on the atmospheric environment in different regions of the globe have been documented in detail by many investigators (e.g., Ropelewski and Halpert 1987; Halpert and Ropelewski 1992). The changes in atmospheric circulation and surface climate (such as air temperature and precipitation) in the North Pacific–North America sector during the warm phase of ENSO have also been contrasted against their counterparts in the cold phase by Hoerling et al. (1997, 2001). Their observational and model results illustrate that the ENSO responses exhibit both linear (with signals in warm events being exactly the opposite of those in cold events) and nonlinear characteristics. The nonlinear behavior includes spatial shifts between the anomaly centers in the warm and cold phases, as well as differences in the degree of proportionality of the signal strength to the magnitude of the SST forcing in El Niño and La Niña events.

Another potentially important contributor to climate variability over North America is the SST forcing in the Indian Ocean–Western Pacific (IWP) sector. Kumar et al. (2001), Kumar and Hoerling (2003), and Lau et al. (2005, hereafter L05) have presented observational and modeling evidence for the substantial role of warm SST anomalies in the IWP region in sustaining the warm and dry conditions over North America in the boreal summer after the mature phase of El Niño events. These SST changes in IWP are partially driven by fluctuations in the overlying atmospheric circulation, which are in turn remote responses to ENSO forcing originating from the central and eastern equatorial Pacific. Details

Corresponding author address: Ngar-Cheung Lau, NOAA/Geophysical Fluid Dynamics Laboratory, Princeton University, Forrestal Campus, P.O. Box 308, Princeton, NJ 08542.
E-mail: gabriel.lau@noaa.gov

DOI: 10.1175/2007JCLI1899.1

of the chain of processes associated with this "atmospheric bridge" mechanism have been described by Klein et al. (1999) and Alexander et al. (2004). In addition to such interannual changes induced by ENSO, the SST field in IWP also exhibit pronounced variability on much longer time scales. Particularly noteworthy is the rising SST in this region during the twentieth century [e.g., see Vecchi and Soden (2007) and the observed SST trend to be presented in our Fig. 1a]. Hoerling and Kumar (2003) pointed out that the multiyear warm condition in IWP after 1998, which is a manifestation of this secular warming trend, may be linked to prolonged droughts and heat waves in many subtropical and midlatitude regions, including North America. To underscore the marked influences of the SST forcing from IWP and other tropical sites, these authors have referred to the tropical oceans as the "perfect ocean for drought."

Diagnoses of observational data as well as output from model experiments by Hoerling and Kumar (2003), L05, and Lau et al. (2006, hereafter L06) reveal that the 200-mb height anomalies accompanying SST variations in IWP are characterized by a notable degree of zonal symmetry, thus leading to widespread impacts of this SST forcing on the climates of many remote regions. The atmospheric signals generated by SST forcing in IWP are discernible in all seasons, with slightly higher amplitudes in the cold portion of the seasonal cycle. Hoerling and Kumar (2003) and L06 have also considered scenarios in which SST forcings associated with both ENSO in the tropical Pacific and secular warming in IWP are present.

In the present study, a concerted effort is made to explore in detail the above-mentioned interplay between the SST forcings in IWP and those in the eastern-central tropical Pacific. Our primary goal is to delineate both the separate and combined roles of the SST warming in IWP and the opposite phases of ENSO in climate variability over North America. Emphasis is placed on the atmospheric responses in the boreal winter season, when both ENSO-related SST changes in the tropical Pacific and their teleconnections with the North American flow pattern attain maximum strength (Rasmusson and Carpenter 1982; Trenberth et al. 1998; Nigam 2003). An extensive suite of model integrations have been conducted to pinpoint the atmospheric signals generated by SST anomalies prescribed at various sites of interest. Our investigation is facilitated by the advent of a new generation of model tools at the Geophysical Fluid Dynamics Laboratory (GFDL), and by the execution of a coordinated set of integrations with large (30) ensemble sizes, which yield statistically robust signals.

The model experiments and observational datasets analyzed in this study are described in section 2. Long-term changes in the circulation patterns related to ENSO episodes during the past and future 50-yr periods are documented in section 3. The responses of the model atmosphere to El Niño and La Niña forcings are compared with the observations in section 4. The model sensitivity to SST warming prescribed in the IWP region is examined in section 5. The model signals corresponding to various combinations of IWP and ENSO forcings are considered in section 6, and an assessment is made on the degree of additiveness of the responses to the individual forcings. Results for the boreal summer season are shown in section 7. Finally, some outstanding scientific issues are discussed in section 8.

2. Experimental design and analysis procedures

a. Experiments with coupled models

We have examined the output from the following two experiments with the 2.1 version of the coupled atmosphere–ocean general circulation model (CM2.1) at the GFDL. The detailed specifications of this model have been documented by Delworth et al. (2006). Both experiments have been conducted as part of our contribution to the 2007 Fourth Assessment Report (AR4) coordinated by the Intergovernmental Panel for Climate Change (IPCC).

1) C20C EXPERIMENT

This experiment is aimed at reproducing the climate variations occurring within the twentieth century. Temporal evolution of various forcings of natural origin (solar irradiance and volcanic aerosols) and due to anthropogenic causes (atmospheric loadings of carbon dioxide, methane, nitrous oxide, halons, ozone, sulfate aerosols, and black and organic carbon; as well as surface cover types) has been inserted in the model framework throughout the past century. Five parallel model runs have been completed using this design. We have focused on the simulation in the 1951–2000 period.

2) A1B EXPERIMENT

This experiment is similar to the C20C runs, except that the projected anthropogenic forcing for the twenty-first century has been used, in accordance with the A1B case in the Special Report on Emissions Scenarios (SRES) adopted by IPCC (Nakićenović et al. 2000). It is estimated that the atmospheric loading of carbon dioxide would be approximately doubled by 2100 under this scenario. Ten individual members have been assembled for the 2001–50 period.

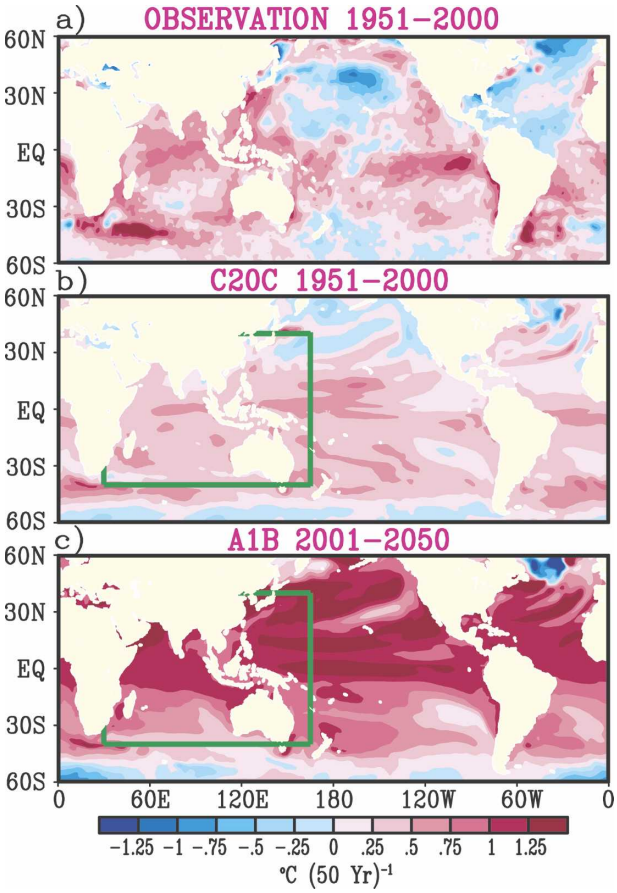

FIG. 1. Distributions of the change in SST over a 50-yr period corresponding to the linear trend as estimated using (a) observations and (b) output from the C20C experiment, both for the 1951–2000 epoch; and (c) output from the A1B experiment for the 2001–50 epoch. Units: °C (50 yr)$^{-1}$. Results are based on 5-month averaged data for the November–March season. The green border in (b) and (c) depicts the boundary of the domain used for prescribing anomalous SST forcing in the T(IWP) sensitivity runs.

The 50-yr SST trends, as simulated in the C20C experiment for the 1951–2000 period, and as projected in the A1B experiment for the 2001–50 era, are compared with the observed trend for the 1951–2000 period in Fig. 1. These trends have been computed by applying a linear regression fit to the data for the 5-month boreal cold seasons (averaged from November to March) in the respective 50-yr time series. For the C20C and A1B experiments, averages have been taken over all available members of the ensemble before performing the trend analysis. Trend patterns for individual runs (not shown) are generally similar to those for the ensemble mean. Observational estimates (Fig. 1a) based on the SST dataset compiled by Hurrell et al. (2008, manuscript submitted to *J. Climate*) indicate warming of more than 0.5°C at most grid points in IWP. The analyses performed by Vecchi and Soden (2007) using the data products of Kaplan et al. (1998) and Smith and Reynolds (2004) also reveal a warming trend in IWP during the twentieth century. The C20C experiment (Fig. 1b) is capable of reproducing this warming in the IWP region, albeit with a weaker trend than observed. The reader is referred to Knutson et al. (2006) for a comprehensive assessment and attribution of the surface temperature trends simulated in this experiment. The corresponding result from the A1B experiment (Fig. 1c) suggests further intensification of this trend, with an additional warming of 1°C or more through the middle of the twenty-first century. Inspection of the SST changes during the 2001–50 period, as projected by individual A1B simulations performed at various model centers participating in the IPCC assessment effort (not shown), reveals that a large majority of these models (15 out of the 19 models being examined) yield warming trends in the IWP sector comparable to those shown in Fig. 1c. The remaining 4 members of this 19-model group also project SST warming in most parts of the IWP region, but with comparatively weaker amplitudes. Many of the IPCC simulations also indicate that IWP region exhibits some of the earliest signals of stable change in surface air temperature (Kattsov and Sporyshev 2006). Since the SST sensitivity runs to be described in section 2b are performed using the GFDL model, we shall henceforth focus our attention on the effects of IWP warming as generated in the C20C and A1B experiments based on the GFDL model only, instead of considering the SST forcing produced by the ensemble of models contributing to the IPCC effort.

b. SST sensitivity runs with the atmospheric GCM

A variety of integrations have been made specifically for this study, so as to delineate the sensitivity of the model atmosphere to different SST forcing patterns. All of the following model runs have been performed on the basis of SST information extracted from each of the C20C and A1B experiments. They entail the prescription of SST data as lower boundary conditions of atmospheric GCMs. The model being used for this purpose is the atmospheric component of CM2.1. This atmospheric model uses the finite-volume formulation (Lin 2004), and has a meridional and zonal resolution of 2° and 2.5°, respectively. For each experiment and each type of SST forcing, an ensemble of 30 individual runs initiated from independent atmospheric conditions have been conducted. We shall henceforth refer to the following integrations as *SST sensitivity runs*, so as to distinguish them from the C20C and A1B *experiments* described in section 2a.

1) CLIMATOLOGICAL (C) RUNS

Computation of anomalous atmospheric responses to perturbed SST forcings requires knowledge of the reference atmospheric condition corresponding to climatological ocean forcing. This "normal" basic state has been estimated by prescribing the annual (12 month) march of long-term-averaged SST data at the lower boundary of the atmospheric GCM. The climatological seasonal cycle of the SST field for each of the C20C and A1B experiments has been obtained by averaging the data for a given calendar month over the 50-yr duration and over all available members of that experiment. As can be expected from the general warming trend during the 1951–2050 period, the climatological SST values for the A1B experiment are higher than those for the C20C experiment (typically by 0.5°–1°C) in most parts of the World Ocean, except in the northwestern Atlantic near 50°N and the Southern Ocean along 60°S. The difference chart between the A1B and C20C climatologies (not shown) is qualitatively similar to the trend pattern in Fig. 1c.

2) EL NIÑO (EN) AND LA NIÑA (LN) RUNS

The typical evolution of the SST anomaly in El Niño and La Niña events in different experiments has been obtained using a composite procedure. The model-generated ENSO events have been identified by computing the 5-month running mean of the SST anomaly[1] averaged over the Niño-3.4 region (5°S–5°N, 120°–170°W), and requiring that this index be larger than 0.4°C (for El Niño) or less than −0.4°C (for La Niña) for 6 consecutive months or longer.[2] These criteria yield altogether 54 warm and 56 cold events in the 5-member ensemble of the C20C experiment for 1951–2000, and 115 warm and 128 cold events in the 10 samples of the A1B experiment for 2001–50. For each month in the 18-month period from March of the year of initiation of the events [year (0)] to August of the following year [year (1)], averages were then taken of the SST anomalies for all available episodes, using the detrended data as described in footnote 1. This composite procedure has been conducted separately for warm and cold events. By including SST anomalies situated outside of the tropical Pacific, we have taken into consideration the oceanic changes induced remotely by ENSO through the atmospheric bridge mechanism.

The composite SST anomalies for El Niño and La Niña events were separately added to the climatological SST data for the corresponding experiment. The 18-month evolution of the perturbed SST forcing was then inserted as lower boundary conditions of the atmospheric GCM. Integrations based on the El Niño and La Niña forcings are referred as EN and LN runs, respectively.

3) IWP TREND [T(IWP)] RUNS

The 50-yr SST increases resulting from the linear warming trend in the IWP sector, as estimated for each calendar month in the C20C and A1B experiments (this procedure is analogous to that for computing the trends for the boreal cold season as shown in Fig. 1), were added to the corresponding climatological SST data for the same calendar month. The perturbed SST field in the 12 months of the annual cycle serves as the boundary forcing for these runs. The forcing domain of 40°S–40°N, 30°–165°E (see green boundaries in Figs. 1b,c) has been used.

4) COMBINATION OF THE IWP TREND AND EL NIÑO OR LA NIÑA [T(IWP)+EN, T(IWP)+LN] RUNS

The combination of SST forcings due to typical El Niño events and the warming trend in IWP has been obtained by summing the SST anomalies used to force the EN and T(TWP) runs separately. Specifically, the global El Niño composite of the SST field in each month of its 18-month life span was added to the 50-yr increase due to secular warming in the IWP domain for the same calendar month. Addition of this total anomaly to the climatological SST field yields the forcing for the T(IWP) + EN runs. Analogously, the T(IWP) + LN runs portray the net effects of composite La Niña events and the long-term warming trend in IWP.

The duration of each realization of the C or T(IWP) runs is 12 months, whereas the time span of a sample of the EN, LN, T(IWP)+EN, and T(IWP)+LN runs is 18 months. The total number of months of model integration required for the above suite of SST sensitivity runs

[1] The SST anomaly was obtained using the following procedure: deviations from the 50-yr-averaged seasonal cycle were first computed. The 121-month running mean of these deviations centered at a given month was then removed from the deviation for that month, so as to remove any long-term trend in the time series.

[2] In a small number of cases, the SST index of a given polarity surpasses the ±0.4°C threshold for 16 consecutive months or longer. These "double-year" events are treated in the following manner: if the extremum of the SST index occurs in January–May of a certain year IYR, this event is assumed to have initiated in the preceding year [i.e., year(0) as defined later in this paragraph is set to be IYR − 1]; if the extremum occurs in August–December of IYR, this event is assumed to have initiated in the same year [i.e., year(0) = IYR]. Events with extremum occurring in June or July are not considered in the present analysis, due to uncertainties of their phasing with the seasonal cycle.

is therefore equal to 2 experiments (C20C, A1B) × 30 samples × (2 scenarios × 12 months + 4 scenarios × 18 months) = 5760. The results to be shown for the sensitivity runs are based on ensemble averages over the available 30 members. (With the exception of Fig. 9, all results in this paper are based on data for the 5-month boreal cold season of November–March.)

The model output has been compared with the corresponding observations for the 1951–2000 era. The observational datasets utilized in this study include reanalyses of 200-mb height and wind at 10-m height (hereafter referred as surface wind), as produced by the National Centers for Environmental Prediction–National Center for Atmospheric Research (NCEP–NCAR; see Kalnay et al. 1996 for details); and surface air temperature and precipitation records over land regions with 0.5° resolution in latitude and longitude, which are archived in the TS 2.1 dataset by the Climate Research Unit (CRU; see Mitchell and Jones 2005)

The statistical significance of various signals of interest has been assessed using the two-tailed Student's *t* test. Anomalies corresponding to the 95% and 99% significance level are indicated by dashed and solid contours, respectively. Purple (orange) contours are used to highlight positive (negative) anomalies.

3. Salient changes in ENSO-related patterns within the 1951–2000 and 2001–50 epochs

As motivation for undertaking the investigations to be described in the following sections, we first present some evidence on the long-term changes in the characteristic patterns associated with El Niño and La Niña that have occurred in the recent past, and that are anticipated in the near future. Two consecutive 50-yr periods have been considered: 1951–2000 and 2001–50. Analyses of the observational records were based on the nine warm episodes initiating in 1957, 1965, 1969, 1972, 1976, 1982, 1987, 1991, and 1997, and the nine cold episodes initiating in 1954, 1955, 1964, 1970, 1973, 1975, 1988, 1998, and 1999. For the C20C and A1B experiments, ENSO episodes were selected using the procedures described in section 2. Secular changes in the atmospheric circulation during ENSO were then delineated by contrasting El Niño–La Niña composites for the first 20 yr of the 1951–2000 or 2001–50 period against those for the last 20 yr of the same period. In order to retain the long-term trend embedded in each 50-yr period, all anomalies to be described in this section are defined as departures from the pertinent half-century climatology (i.e., 1951–2000 for reanalysis and C20C data; 2001–50 for A1B data).

The El Niño and La Niña composite patterns of the anomalous 200-mb height in the North Pacific–North American sector, as computed for various 20-yr groups in the observational, C20C, and A1B datasets are assembled in Fig. 2. Inspection of the pair of panels in a given row of this figure reveals that the composite pattern in the beginning decades of the 50-yr period is markedly different from that in the concluding decades of the same period.[3] Such distinctions are particularly evident for features over the North American continent. For El Niño composites (i.e., the top half of Fig. 2), the amplitude of the negative height anomaly over the continental United States is substantially reduced in 1981–2000 or 2031–50 (Figs. 2b,d,f) as compared with that of the corresponding feature in 1951–70 or 2001–20 (Figs. 2a,c,e). Conversely, the anomalous ridge over the same region in La Niña events (i.e., the bottom half of Fig. 2) is much more prominent toward the end of the 50-yr period (Figs. 2h,j,l) than that near the beginning of the same period (Figs. 2g,i,k). The observational and model evidence in Fig. 2 is indicative of the presence of a long-term rising trend in 200-mb height in the subtropical and midlatitude zones of North America in both the 1951–2000 and 2001–50 periods. This positive trend in the height field acts against the negative height anomaly center over North America during El Niño episodes, thus resulting in weakening of the response signals at that site. On the other hand, the same trend contributes to the progressive buildup of a strong ridge anomaly in the U.S. sector during La Niña. For the 1951–2000 period, such interactions between the long-term trend and the ENSO responses, as simulated in the C20C experiment (Figs. 2c,d,i,j), are substantiated by the corresponding observational results based on NCEP–NCAR reanalyses (Figs. 2a,b,g,h). The findings in Fig. 2 imply that, with the passage of time, the underlying upward trend in geopotential height over North America will lead to increasing asymmetry of the local climate response with respect to ENSO polarity, with much stronger signals in the La Niña phase than in the El Niño phase.

Seager et al. (2003) and L06 noted that the trend in geopotential height in the middle or upper troposphere exhibits considerable zonal symmetry. Their findings are further examined in Fig. 3, which shows the latitudinal profiles of composites of the zonally averaged 200-mb height anomaly for El Niño and La Niña in various 20-yr subperiods considered in Fig. 2. For El Niño composites (Figs. 2a,c,e), the negative height

[3] Since different 50-yr climatologies have been removed from the data for the 1951–2000 and 2001–50 periods (see the previous paragraph), it is not meaningful to compare the patterns for 1981–2000 with those for 2001–20 in Fig. 2.

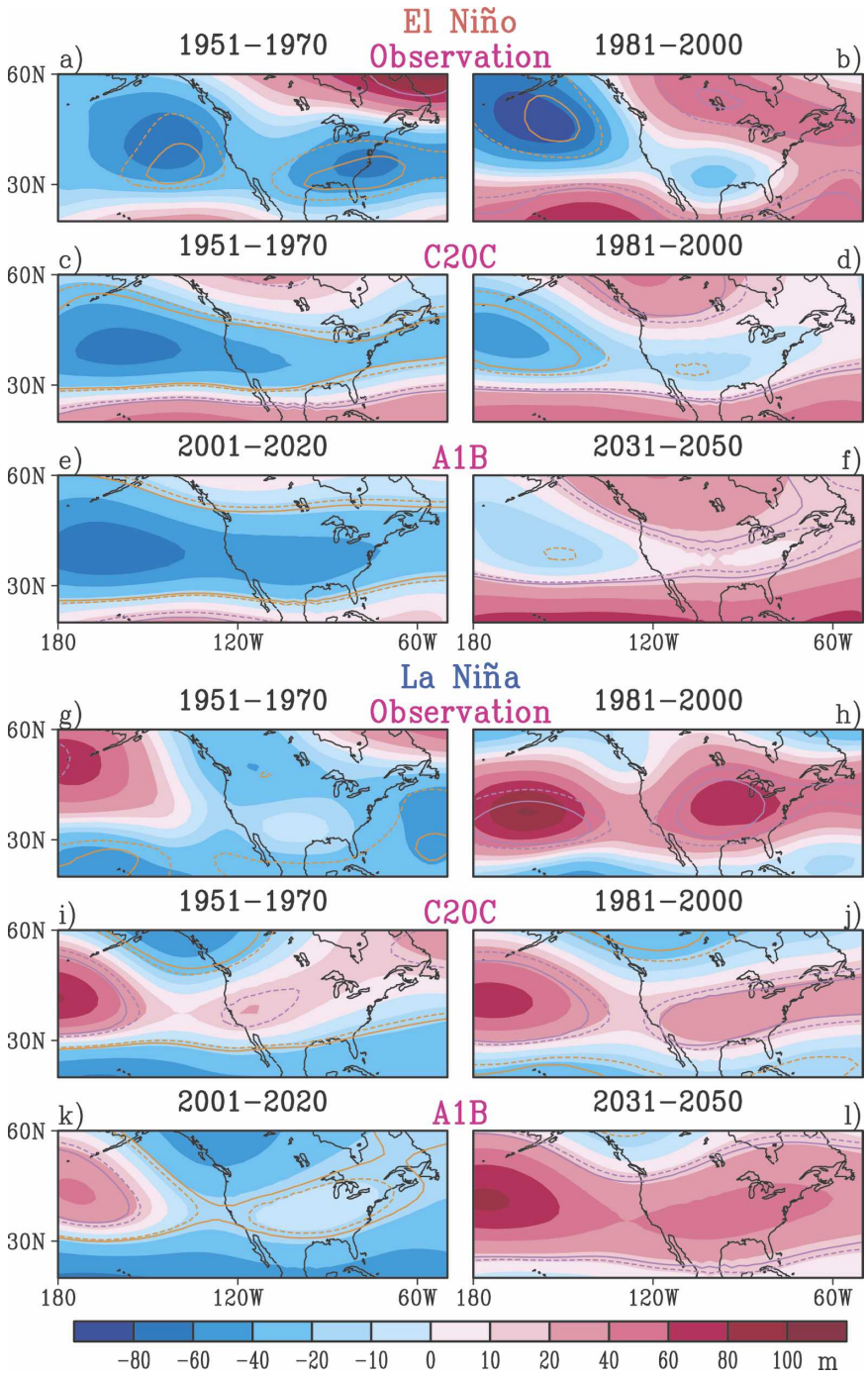

FIG. 2. Distributions of the composites of 200-mb height anomalies in (a)–(f) El Niño and (g)–(l) La Niña events, as constructed using NCEP–NCAR reanalyses for the (a), (g) 1951–70 and (b), (h) 1981–2000 periods; output from the C20C experiment for the (c), (i) 1951–70 and (d), (j) 1981–2000 periods; and output from the A1B experiment for the (e), (k) 2001–20 and (f), (l) 2031–50 periods. All anomalies are defined as departures from the 50-yr climatology of the corresponding dataset (i.e., 1951–2000 for NCEP–NCAR and C20C; and 2001–50 for A1B). Dashed and solid purple (orange) contours denote positive (negative) anomalies at the 95% and 99% significance levels, respectively. With the exception of Fig. 9, the results in all diagrams of this article are based on the 5-month boreal cold season from November to March.

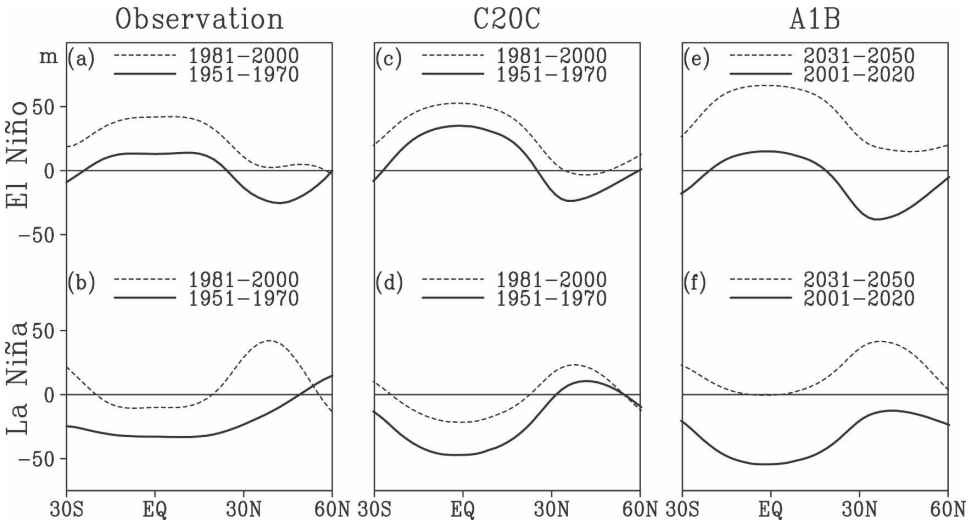

FIG. 3. Latitudinal variations of the composites of zonally averaged 200-mb height anomalies in El Niño (top curves) and La Niña (bottom curves) events, as constructed using (a), (b) NCEP–NCAR reanalyses and (c), (d) output from the C20C experiment, for the 1951–70 (solid curves) and 1981–2000 (dashed curves) periods; and (e), (f) output from the A1B experiment for the 2001–20 (solid curves) and 2031–50 (dashed curves) periods. All anomalies are defined as departures from the 50-yr climatology of the corresponding dataset (i.e., 1951–2000 for NCEP–NCAR and C20C; and 2001–50 for A1B).

anomaly in the northern extratropics during the earlier portion of each 50-yr period (solid curves) is seen to diminish considerably or even become positive toward the end of that period (dashed curves). The notable enhancement of the positive height anomaly in the tropical zone through the 50-yr period may be attributed to the equator-wide oceanic warming trend (see Fig. 1). For La Niña composites (Figs. 2b,d,f), the northern extratropical ridge anomaly is much more prominent in the latter decades of the 50-yr period than in the earlier decades. The tropical negative anomaly is seen to weaken considerably with the passage of time, again on account of SST increase in the equatorial oceans.

It is evident from the results in Figs. 2 and 3 that the rising trend in subtropical and midlatitude geopotential height will play an ascending role in modulating the responses of the North American and zonally averaged climates to the warm and cold phases of ENSO. In the following sections, we shall devote much of our attention to the origin of this "ridging" phenomenon, and the manner in which this trend of increasing heights interacts with interannual variability associated with ENSO fluctuations.

4. Observed and simulated atmospheric responses to ENSO forcing on interannual time scales

The capability of the atmospheric GCM to reproduce the observed responses of the North American climate in typical El Niño and La Niña episodes is assessed in this section. The observational results are based on composites over the nine warm events and nine cold events occurring in the entire 1951–2000 period (see lists in section 3), and have been computed using NCEP–NCAR reanalyses for 200-mb height and surface wind, as well as the CRU TS 2.1 dataset for surface air temperature (SAT) and precipitation. These variables have been chosen to emphasize various aspects of the surface climate over North America that are influenced by ENSO. In order to accentuate the interannual component of these response signals, all anomalies are defined as departures from the 11-yr running mean centered at each ENSO event. The atmospheric model responses to prescribed anomalous SST forcings corresponding to El Niño and La Niña events have been obtained by subtracting the output of the C runs from that of the EN and LN runs, respectively (hereafter referred to as EN-C and LN-C). These differences have been computed for the sensitivity runs subjected to SST boundary conditions derived from each of the C20C and A1B experiments (see section 2).

The wintertime patterns of the observed and simulated anomalies are shown in Fig. 4 for 200-mb height, and in Fig. 5 for SAT, surface wind, and precipitation. Responses to El Niño and La Niña are displayed in the left and right panels of each figure, respectively. Inspection of the panels based on observational data reveals sign reversals of the principal anomalies during opposite phases of ENSO. The westward shift of the ob-

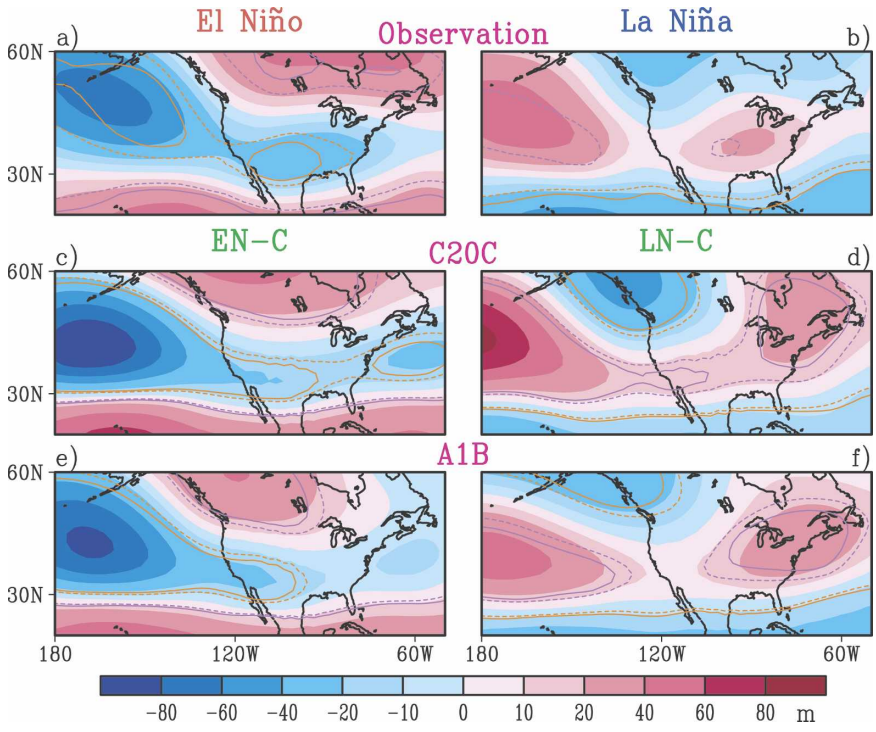

FIG. 4. Distributions of the composites of anomalous 200-mb height over selected (a), (c), (e) El Niño and (b), (d), (f) La Niña events, as constructed using (a), (b) NCEP–NCAR reanalyses, and output from the EN and LN sensitivity runs based on SST forcings from the (c), (d) C20C and (e), (f) A1B experiments. All observed anomalies are defined as departures from the 11-yr running mean centered at each ENSO event. Dashed and solid purple (orange) contours denote positive (negative) anomalies at the 95% and 99% significance levels, respectively.

served anomaly centers over the North Pacific and Canada in the La Niña composite relative to the corresponding features in the El Niño composite, as noted previously by Hoerling et al. (1997), is clearly discernible in Figs. 4a,b. This spatial displacement between the 200-mb height patterns for the warm and cold events is accompanied by similar shifts in the observed anomalies of surface wind circulation and SAT over Canada (Figs. 5a,b). The above-normal SAT poleward of 45°N in observed El Niño events (Fig. 5a) is accompanied by anomalous southerly or onshore flows (see arrows in the same panel); whereas the below-normal temperatures south of 35°N are collocated with anomalous northerly or offshore circulation. The polarity of the SAT changes is reversed at most locations during La Niña years (Fig. 5b), with the cold (warm) conditions prevailing in the northwestern (southeastern) quadrants of the North American landmass. The composite patterns for observed precipitation exhibit more small-scale signals. Notable features in the El Niño chart (Fig. 5g) include the wet conditions along the southern tier of the continental United States and parts of Mexico, and the dry conditions over the Pacific Northwest and parts of the eastern United States. Most of these anomalies change sign during La Niña episodes (Fig. 5h). The essential characteristics of the SAT and precipitation composites, as presented in Figs. 5a,b and 5g,h, are in overall agreement with the observational findings reported by Ropelewski and Halpert (1986, 1989) and Hoerling et al. (1997, 2001) based on other analysis techniques.

A considerable degree of resemblance exists between the model response patterns to SST forcings based on the individual C20C and A1B experiments (Figs. 4c–f, 5c–f, and 5i–l). This finding indicates that ENSO responses in the North Pacific–North American sector are not noticeably affected by alteration of the oceanic and atmospheric background states occurring within the 1951–2050 period. The correspondence between the results for C20C and A1B in Figs. 4–5 also suggests that the composite SST anomaly in ENSO events generated internally in the coupled CM2.1 model under 1951–2000 and 2001–50 settings is similar to each other. This inference has been verified by comparing the composites of SST anomaly patterns in ENSO events appearing in the C20C and A1B experiments (not shown).

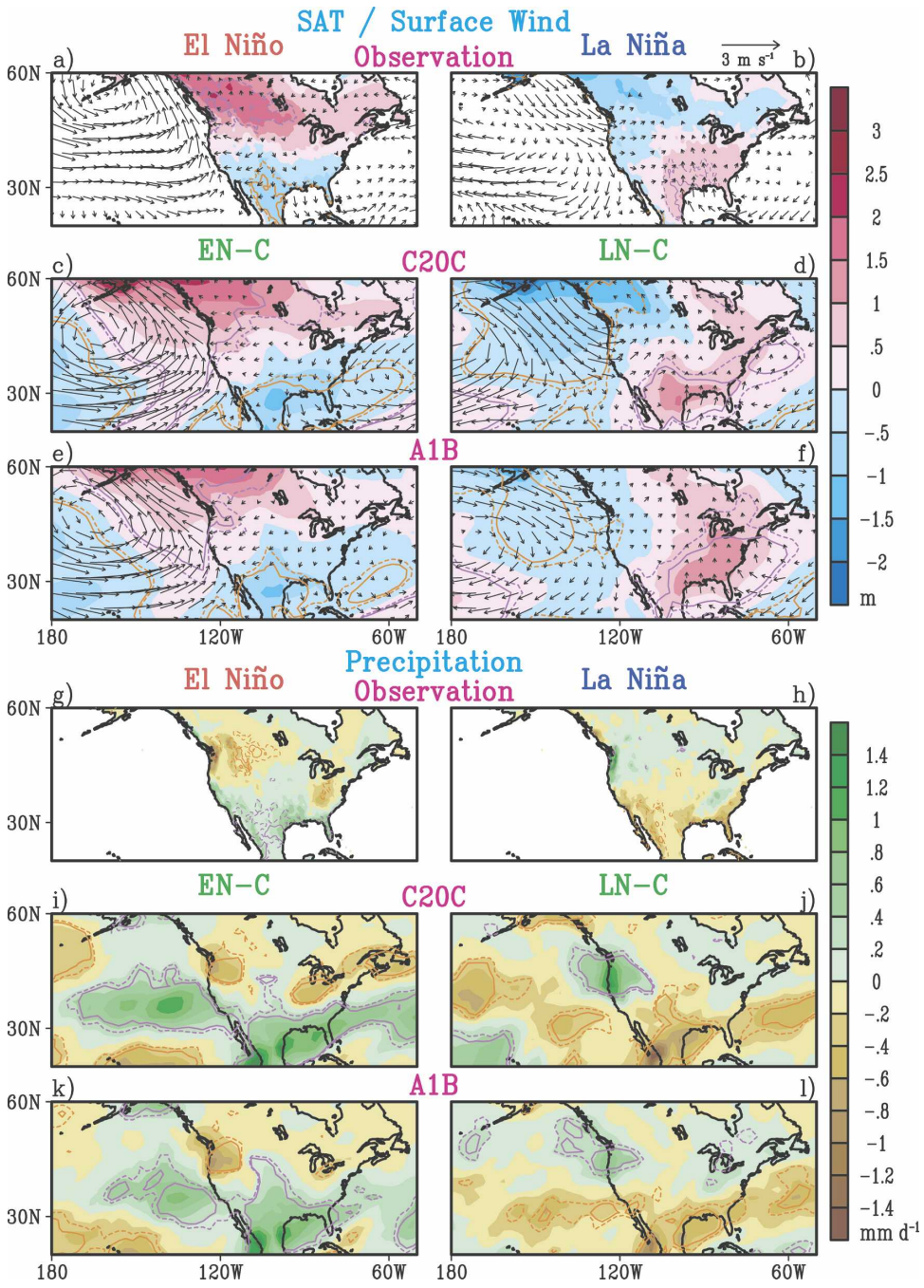

FIG. 5. As in Fig. 4, but for composites of anomalous (a)–(f) SAT (shading) and surface wind (arrows), and (g)–(l) precipitation. (a), (b), (g), (h) Observational results are based on NCEP–NCAR reanalyses for surface wind, and the CRU TS 2.1 dataset for SAT and precipitation. Model results are based on EN and LN sensitivity runs associated with the (c), (d), (i), (j) C20C and (e), (f), (k), (l) A1B experiments.

The principal features of the simulated patterns in Figs. 4 and 5 are in overall agreement with their observed counterparts. In particular, the polarity of the anomalies in EN-C (left panels) is opposite to that in LN-C (right panels), with discernible westward displacements of the 200-mb height and SAT patterns for La Niña relative to those for El Niño. The model atmosphere is apparently capable of reproducing some of the regional characteristics of the observed precipitation responses to ENSO. For instance, the observed wet conditions along the California and Gulf coasts, and the dryness over the Pacific Northwest and south of the

Great Lakes region during El Niño, as well as the reversal of these anomalies during La Niña (see Figs. 5g–h), are also seen in the corresponding model results (Figs. 5i–l). Wittenberg et al. (2006) have also documented the fidelity of the ENSO simulations by the CM2.1 model.

Composite anomaly charts of the same set of variables displayed in Figs. 4 and 5 have also been compiled using the output for individual El Niño and La Niña events as simulated by the coupled GCM in each of the C20C and A1B experiments. These results (not shown) bear a strong resemblance to the anomalies generated by the sensitivity runs in response to the composite El Niño and La Niña forcings, as presented in Figs. 4 and 5. The spatial correlation coefficients between the responses in the EN or LN runs, and the corresponding ENSO composites based on output from C20C and A1B, are mostly within the ranges of 0.8–0.9 for the 200-mb height and SAT fields, and 0.7–0.8 for precipitation.[4] Such strong correlations imply that the ENSO-related atmospheric signals over the North Pacific–North America in the C20C and A1B experiments are mostly attributable to influences of SST forcings based on these experiments, as incorporated in the design of the EN and LN sensitivity runs. This finding suggests that the remote responses as portrayed in Figs. 4 and 5 are not critically dependent on the two-way atmosphere–ocean coupling associated with ENSO. Hence, we could use with confidence the solutions of the EN and LN runs as the surrogate of the ENSO responses simulated in their corresponding "parent" experiment based on the coupled GCM.

5. Atmospheric responses to the long-term warming trend in IWP

We next turn our attention to the effects of the secular warming in the IWP sector on the model atmosphere, as simulated in the T(IWP) runs (see section 2b). The distributions of 200-mb height, SAT, surface wind, and precipitation as obtained by subtracting the model climatology (C runs) from the T(IWP) runs, are displayed in Fig. 6 for SST forcings based on each of the C20C and A1B experiments.

The patterns for 200-mb height (Figs. 6a,b) are dominated by a positive anomaly that extends across much of the zonal belt centered near 45°N. A possible mechanism contributing to this anomalous ridge has been proposed by L05 and L06. These studies indicate that SST variations in IWP alter the meridional temperature gradient over the Eurasian continent and the western Pacific. This change in baroclincity affects the structure of the local background flow, and thereby modulates the location and intensity of eastward propagating synoptic-scale disturbances. The perturbed momentum transports associated with these anomalous "storm-track" activities in turn influence the quasi-stationary circulation in the eastern portion of the North Pacific as well as the North American sectors. Figures 6c,d show that the enhanced upper-tropospheric ridge is accompanied by two anomalous anticyclonic circulation centers near the surface, one situated over the northeastern North Pacific, and the other off the eastern seaboard of North America. The Pacific center is associated with anomalous northerly surface flow along much of the west coast of North America, which brings about below-normal temperatures to that region. The southerly flow to the west of the Atlantic anticyclone leads to warm conditions over the eastern United States. Dry anomalies prevail on the southern or eastern flanks of the Pacific anticyclone, as well as the southern and western portions of the Atlantic anticyclone (Figs. 6e,f). Positive precipitation changes are seen to the north or northwest of these anomalous circulation centers. The interrelationships between different meteorological fields, as portrayed in Fig. 6, are reminiscent of those between analogous patterns simulated in an experiment subjected to time-varying global SST forcing observed during the 1998–2002 period, when marked warming also occurred in the IWP sector (L06). That earlier study has also noted that westerly (easterly) anomalies are accompanied by enhanced (reduced) synoptic-scale activities, thus leading to positive (negative) precipitation changes. The correspondence between the signals in zonal wind and those in precipitation is also evident from Figs. 6c–f.

The results in Fig. 6 indicate that the response to imposed SST forcing based on the A1B experiment (right panels) is stronger than that to SST changes simulated in the C20C experiment (left panels). This finding is apparently related to the relative intensity of the warming trends generated in these two experiments (cf. Fig. 1b with Fig. 1c). The local precipitation responses to oceanic warming prescribed in IWP may be

[4] The statistical significance of these spatial correlation coefficients has been assessed by processing the output from a 300-yr control experiment with the CM2.1 model subjected to constant 1990 radiative forcing. Altogether 150 samples, each containing a set of 30 randomly selected winters, were drawn from this dataset. (The sample size of 30 is the same as that of the SST sensitivity runs described in section 2b.) Spatial correlation coefficients were computed between all possible distinct pairings of these sample means, yielding a total population of $150 \times 149 \div 2 = 11\,175$ values. Threshold values at various percentiles were then noted. This testing procedure indicates that the correlations as cited in the main text all surpass the 99th percentile of the population.

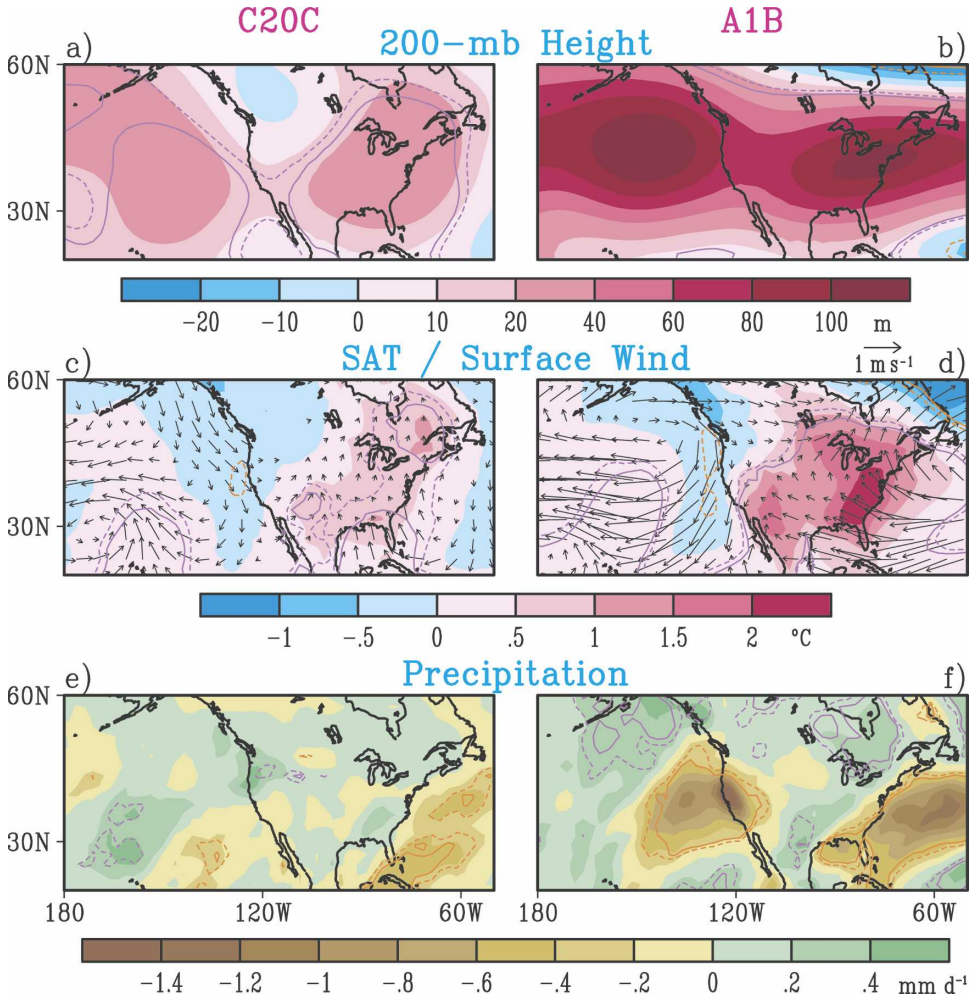

FIG. 6. Distributions of the model responses to the 50-yr SST change in the IWP sector, as simulated in the T(IWP) sensitivity runs based on SST trends obtained from the (a), (c), (e) C20C and (b), (d), (f) A1B experiments. Anomalous patterns are shown for (a), (b) 200-mb height; (c), (d) SAT (shading) and surface wind vector (arrows); and (e), (f) precipitation. Dashed and solid purple (orange) contours denote positive (negative) anomalies at the 95% and 99% significance levels, respectively.

inferred from charts analogous to those in Figs. 6e,f, but plotted for the IWP sector (not shown). The precipitation changes in the IWP region, as simulated by the T(IWP) runs for the A1B experiment, are larger than their counterparts in the T(IWP) runs for the C20C experiment. For both A1B and C20C experiments, the precipitation response near the equatorial zone of IWP during the boreal cold season is characterized by positive (negative) changes south (north) of the equator. This pattern appears to bear a stronger spatial correlation with the distribution of the total SST field (i.e., sum of climatology and warming trend, with increasing temperatures from north to south across the equator during boreal winter), than with the distribution of the warming trend alone (see Figs. 1b,c). Further study is needed to delineate the linkage of the precipitation signals in the IWP sector to the underlying SST conditions in different phases of the annual cycle.

The atmospheric responses to secular warming in IWP (Fig. 6) may be contrasted with those associated with ENSO forcing, as simulated in the EN and LN runs (Figs. 4 and 5). The anomalies generated by IWP warming have the same polarity as those in response to La Niña (right panels of Figs. 4 and 5), and the opposite polarity as the corresponding features in the charts for El Niño (left panels of Figs. 4 and 5). These qualitative impressions have been substantiated by computing the spatial correlation coefficients between the patterns for T(IWP)-C and EN-C, as well as between the results from T(IWP)-C and LN-C, based on SST forcings for

TABLE 1. Spatial correlation coefficients between the patterns of selected variables for (first row) T(IWP)-C and EN-C and (second row) T(IWP)-C and LN-C. Results for sensitivity runs based on SST forcings derived from the C20C (A1B) experiments are displayed in the left (right) half of the table. Computations are based on the domain of 20°–60°N, 180°–50°W. Statistical significance of the correlation coefficients are assessed using the procedure outlined in footnote 4. Correlation values surpassing the 90%, 95%, and 99% confidence levels are shown using bold italic, underlined bold italic, and underlined bold italic followed by an asterisk, respectively.

	C20C			A1B		
	200-mb height	SAT	Precipitation	200-mb height	SAT	Precipitation
T(IWP)-C vs EN-C	−0.56	***−0.48***	0.05	***−0.66***	−0.33	***−0.27***
T(IWP)-C vs LN-C	***0.64***	***0.79****	***0.39***	***0.61***	***0.80****	***0.73***

each of the C20C and A1B experiments. These statistics are displayed in Table 1. For pairings between T(IWP)-C and LN-C (second row), the spatial correlations are uniformly positive. The correlation values for the SAT and precipitation fields are significant at the 99% and 95% levels, respectively. Conversely, the correlations between the charts for T(IWP)-C and EN-C (first row) are mostly negative. The evidence presented here lends further support to the joint effects of IWP warming and La Niña on the enhanced meteorological anomalies observed in the 1998–2002 period, as documented in L06.

6. Combined impacts of IWP warming and ENSO

The cumulative effects of the warming trend in the IWP sector and the two opposite phases of ENSO may be assessed by examining the output from the T(IWP)+EN and T(IWP)+LN runs, as described in section 2b. The responses of various atmospheric fields in these runs are illustrated in Fig. 7.

For a given variable and SST forcing from a given experiment, the amplitudes of the anomalies in the T(IWP)+LN runs are mostly higher than those in the T(IWP)+EN runs. This finding is again indicative of the in-phase (out of phase) relationships between the effects of La Niña (El Niño) and IWP warming, as noted in the previous section. The disparity in signal strengths simulated in the T(IWP)+EN and T(IWP)+LN runs is most evident for SST forcings based on the A1B experiment, in which the SST in the IWP sector exhibits the strongest trend (see Fig. 1c). The relatively weaker SST trends simulated in the C20C experiment (Fig. 1b) leads to less modulation of the responses to ENSO by the forcing in the IWP region. As an objective domain-wide measure of the amplitudes of the anomalies appearing in individual panels in Fig. 7, the areal mean of squares of the departures of the anomalies at each grid point from the domain average was computed, and the square root of this mean was then taken. All calculations are based on the domain of 20°–60°N, 180°–50°W. The ratio of this root-mean-square (rms) measure for the T(IWP)+LN-C pattern relative to the rms measure for T(IWP)+EN-C pattern, as computed using sensitivity runs based on SST forcing from the A1B experiment, is displayed in the first row of Table 2. This ratio exceeds unity for all three variables being considered. Our analysis hence confirms that, in the presence of IWP warming projected for the twenty-first century, the simulated strengths of atmospheric anomalies are higher in La Niña events than in El Niño events.

Comparison between the patterns in Fig. 7 and the corresponding panels in Figs. 4 and 5 suggests that many of the anomalies in the LN runs become much stronger in T(IWP)+LN. For sensitivity runs based on the A1B experiment, the ratios of the rms measure (see definition in the preceding paragraph) for the T(IWP)+LN-C pattern relative to the same measure for LN-C are shown in the second row of Table 2. These statistics indicate that the mean amplitudes of the local features in T(IWP)+LN-C are significantly higher than those in LN-C. On the other hand, the patterns for T(IWP)+EN-C and EN-C are suggestive of negative interference between responses to IWP warming and to El Niño. In some instances, this interference becomes so strong that the polarity of some anomalies in the EN runs is reversed in the T(IWP)+EN runs. For instance, the anomalous 200-mb trough over the North Pacific in EN based on the A1B experiment (Fig. 4e) is replaced by a weak positive height anomaly over the same location in T(IWP)+EN (Fig. 7b). These contrasts between Figs. 4, 5, and 7 are in accord with the aforementioned relationships between responses to ENSO and those to warming in IWP.

The anomaly patterns presented in this and the preceding two sections are strongly supportive of the notion that the net response to both IWP and ENSO forcings, as obtained from the T(IWP)+EN and T(IWP)+LN runs (Fig. 7), may be approximated as the linear sum of the separate responses to forcings associated with IWP warming (Fig. 6) and El Niño/La Niña (Figs. 4 and 5). This impression has been tested by adding the anomalous pattern based on the T(IWP) run to that based on the LN or EN run, and then comparing the result with

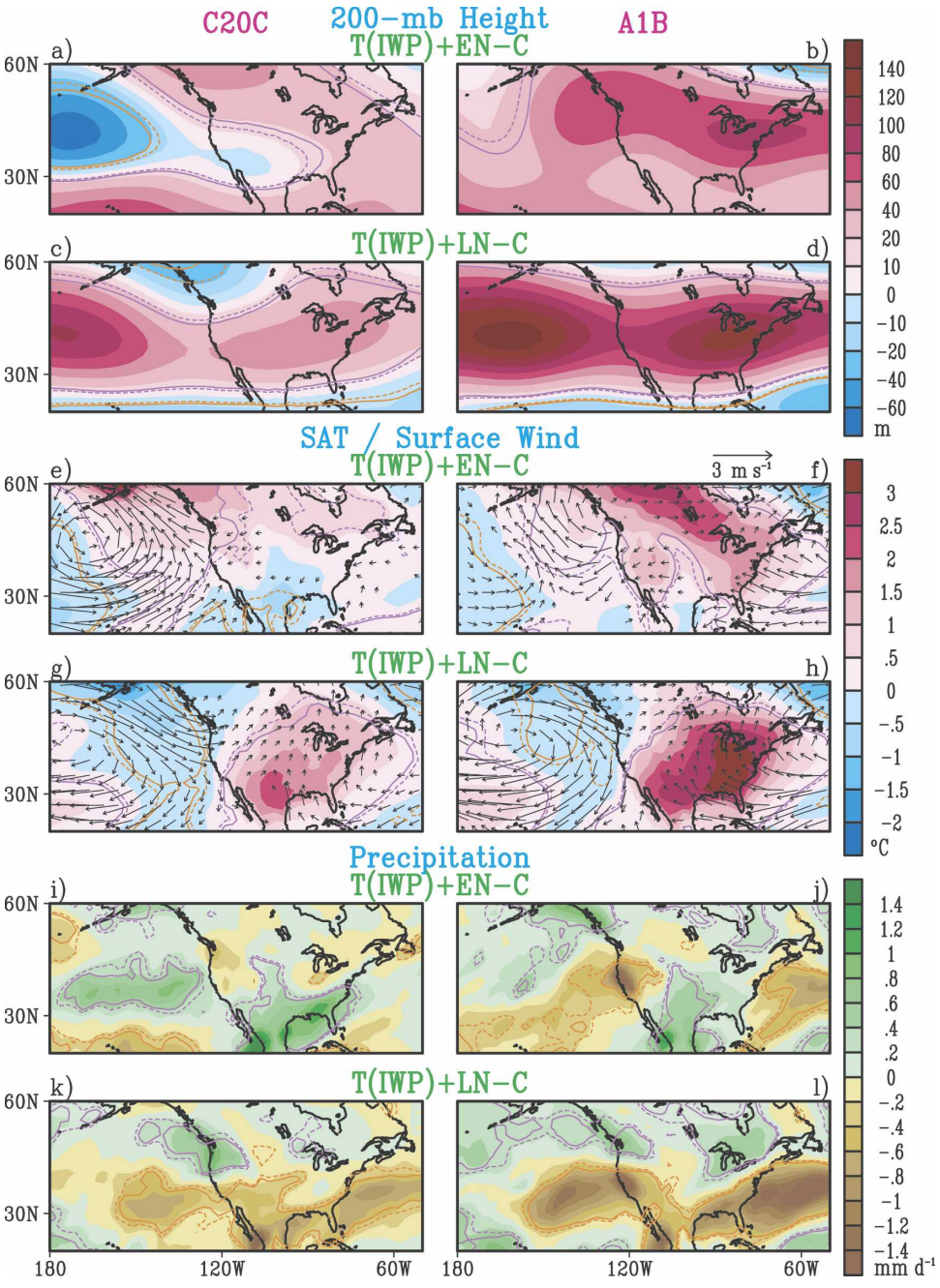

FIG. 7. Distributions of the model responses to combined SST forcings due to both ENSO and the secular warming trend in IWP, as obtained by subtracting the output of the C runs from that of the T(IWP)+EN or T(IWP)+LN runs associated with the (a), (c), (e), (g), (i), (k) C20C and (b), (d), (f), (h), (j), (l) A1B experiments. Results are shown for (a)–(d) 200-mb height, (e)–(h) SAT (shading) and surface wind (arrows), and (i)–(l) precipitation. Dashed and solid purple (orange) contours denote positive (negative) anomalies at the 95% and 99% significance levels, respectively.

the pattern based on the T(IWP)+EN or T(IWP)+LN run. This checking procedure has been conducted for all atmospheric variables of interest and for SST forcings based on each of the C20C and A1B experiments. The results of this analysis confirm that the sum of the responses to individual IWP and ENSO forcings (not shown) bear a strong resemblance to the response to the combined IWP and ENSO forcings (shown in

TABLE 2. Ratios of the rms measure (see definition in section 6) for the T(IWP)+LN-C pattern relative to the rms measure for the (first row) T(IWP)+EN-C pattern and (second row) LN-C pattern. All sensitivity runs are based on the A1B experiment. Statistical significance of these ratios has been assessed by computing the ratios of rms measures for 11 175 pairs of 30-yr samples randomly drawn from a 300-yr control integration (see details of the sampling strategy in footnote 4). Entries in this table surpassing the 90th, 95th, and 99th percentiles of the population thus assembled are shown using bold italic, underlined bold italic, and underlined bold italic followed by an asterisk, respectively.

	A1B		
	200-mb height	SAT	Precipitation
T(IWP)+LN-C vs T(IWP)+EN-C	***2.07***	1.43	***1.53***
T(IWP)+LN-C vs LN-C	***2.47***	***2.37****	***2.27****

Fig. 7), with spatial correlation coefficients mostly lying within the 0.8–0.9 range, which surpasses the 99% confidence level as determined by the testing procedure described in footnote 4.

The zonally averaged atmospheric responses to IWP warming and ENSO are portrayed in Fig. 8 for SST forcings based on the A1B experiment. This figure shows the latitudinal profiles of the anomalous zonal mean 200-mb height as simulated in the sensitivity runs for T(IWP) (top curve), EN and T(IWP)+EN (middle solid and dashed curves, respectively), and LN and T(IWP)+LN (bottom solid and dashed curves, respectively). The linear sum of the individual responses in the T(IWP) and EN runs is also displayed as a dotted curve in the middle part of the figure. Similarly, the sum of the responses in the T(IWP) and LN runs is shown as a dotted curve in the bottom part. These dotted curves are to be compared with the responses in the T(IWP)+EN or T(IWP)+LN runs (dashed curves).

The top curve in Fig. 8 indicates that IWP warming in the A1B experiment generates enhanced ridges centered at the equator and the 30°–40°N belt. The zonal mean responses to ENSO are characterized by anomalous ridges in the tropics and troughs in midlatitudes during warm events (middle solid curve), and height fluctuations of reversed polarity during cold events (bottom solid curve). The mechanisms contributing to the extratropical zonal mean signals in the T(IWP), EN, and LN runs have been examined by Seager et al. (2003), L05, and L06 by diagnosing various zonally averaged quantities along the meridional plane. These investigations illustrate that the perturbed SST conditions modify the zonal mean flow as well as eddy momentum transports. The altered transient eddy forcing in turn affects the location and intensity of the zonal mean meridional overturning circulations in the extratropics,

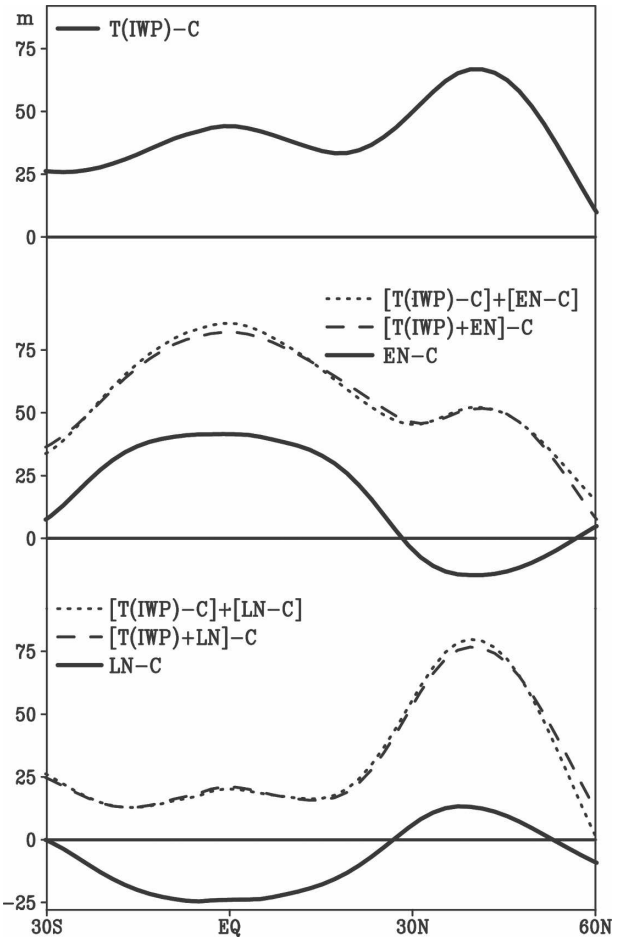

FIG. 8. Latitudinal variations of the model responses in zonally averaged 200-mb height, as simulated in the T(IWP) (top curve), EN and T(IWP)+EN (middle solid and dashed curves, respectively), and LN and T(IWP)+LN (bottom solid and dashed curves, respectively) sensitivity runs based on SST forcings derived from the A1B experiment. The sums of the individual responses in the T(IWP) and EN runs, and in the T(IWP) and LN runs, are depicted using dotted curves in the middle and bottom parts of this figure, respectively. All responses are obtained by subtracting the output of the C run from that of the sensitivity runs.

and thereby influence the structure of the temperature and geopotential height fields in the middle latitudes. In the northern extratropics, the enhanced ridge due to IWP warming is in phase with the La Niña response, and out of phase with the El Niño signal. These relationships are consistent with the response to the combined IWP and ENSO forcings in the T(IWP)+LN and T(IWP)+EN runs. As is evident from the bottom dashed curve in Fig. 8, the combined forcings yield a prominent ridge anomaly centered at 40°N during La Niña. On the other hand, the polarity of the trough anomaly in the same location during El Niño events

(middle solid curve) is switched in the presence of IWP warming (middle dashed curve), and an anomalous ridge of moderate strength emerges in midlatitudes. The long-term changes of the El Niño and La Niña composites of zonal mean 200-mb height, as described in Figs. 3e,f for the 2001–50 period in the A1B experiment, may partially be attributed to the interactions between responses to ENSO and to IWP warming, as inferred from the evidence displayed in Fig. 8.

The close agreement between the dashed and dotted curves in Fig. 8 confirms that the zonal mean response to the combined IWP and ENSO forcings (as produced by the T(IWP)+EN and T(IWP)+LN runs) may be approximated by separately modeling the effects due to IWP warming [T(IWP) runs] and ENSO (EN or LN runs), and then adding the two results.

Latitudinal profiles of responses of the zonally averaged 200-mb height have also been plotted using output from various sensitivity runs based on SST forcings from the C20C experiment (not shown). The anomalous ridge in the northern extratropics in response to IWP warming as simulated in C20C experiment is less prominent than the corresponding feature associated with the A1B experiment (see upper curve in Fig. 8). In analogy with the findings presented in Fig. 8, the C20C results indicate that this ridge reinforces the midlatitude response to La Niña, and opposes the response to El Niño. The linear superposition of the separate effects of IWP warming and ENSO is also evident in the T(IWP)+EN and T(IWP)+LN runs based on the C20C experiment.

7. Responses to IWP warming in the boreal warm season

We have thus far focused our attention on atmospheric signals in the northern cold season. Parallel diagnoses have been conducted on the output from the sensitivity runs for the boreal warm season. The latter results (not shown) indicate that the 200-mb height and surface wind responses to ENSO in the summers of both year (0) and year (1) are considerably weaker than those in the cold season straddling the two years (see Figs. 4 and 5). For summertime SST forcings based on the A1B experiment, the amplitudes of ENSO responses in all atmospheric fields considered in this study are also smaller than those simulated in the T(IWP) runs. As a consequence, the main features in the anomalies generated by the T(IWP)+EN and T(IWP)+LN runs in the warm season are dominated by the responses to IWP warming alone. Hence, we shall only present the results from the T(IWP) runs for the warm season in this section.

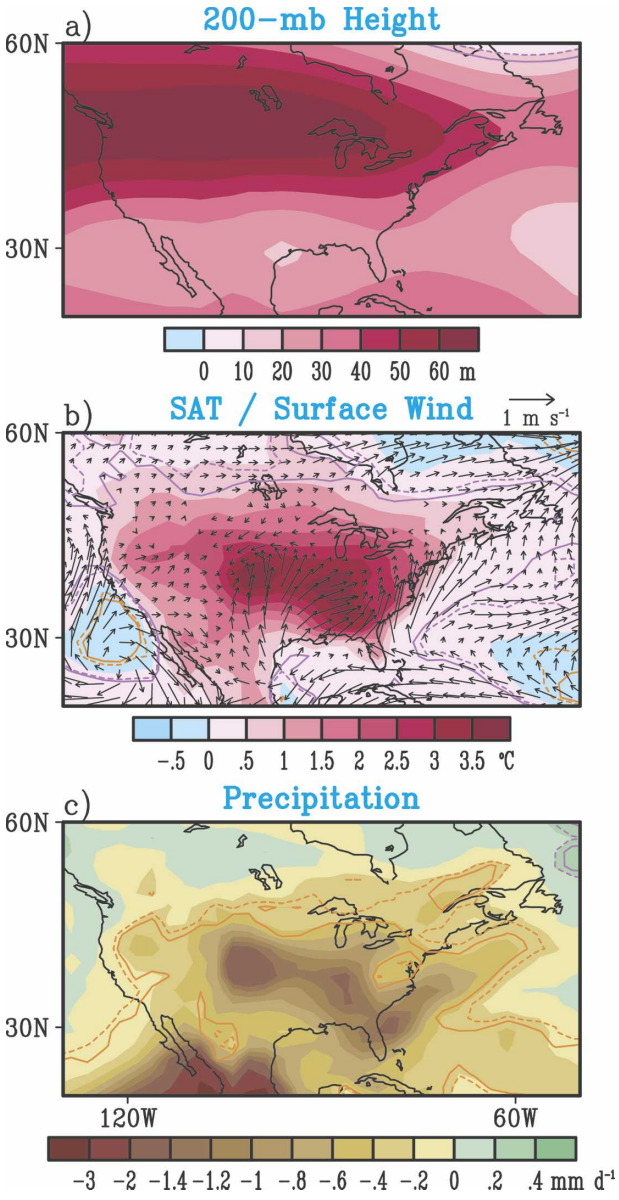

FIG. 9. Distributions of the model responses in the 5-month boreal warm season from May to September to the 50-yr SST change in the IWP sector, as simulated in the T(IWP) sensitivity runs based on SST trends projected in the A1B experiment. Anomalous patterns are shown for the (a) 200-mb height, (b) SAT (shading) and surface wind vector (arrows), and (c) precipitation. Dashed and solid purple (orange) contours denote positive (negative) anomalies at the 95% and 99% significance levels, respectively. Note that the 200-mb height anomalies in almost the entire domain surpass the 99% significance level.

The distributions of the anomalous patterns generated by the T(IWP) runs based on A1B forcings for the May–September season are shown in Figs. 9a,b,c, for 200-mb height, SAT and surface wind, and precipitation, respectively. The projected SST trend in IWP dur-

ing this season (not shown) is comparable to that for the boreal cold season (see Fig. 1c). The local precipitation response in IWP to this SST trend in boreal summer (not shown) is dominated by positive (negative) changes north (south) of the equator. This pattern is apparently linked to the meridional gradient of the underlying total SST field, in analogy with the situation for boreal winter (see discussion in section 5). Positive 200-mb height anomalies are simulated throughout the North American domain, with a zonally elongated maximum being located over the U.S.–Canadian border. A near-surface cyclonic circulation center is discernible over the central United States, just to the south of the upper-tropospheric ridge. This configuration of 200-mb height and surface wind responses is suggestive of a "warm-core" structure over the continental interior. Also evident in Fig. 9b are the southerly and southwesterly flows on the western flank of the anomalous anticyclone over the subtropical Atlantic and Gulf of Mexico. This circulation pattern is accompanied by warm and dry conditions over much of the continental United States (Figs. 9b,c). The features portrayed in Fig. 9 bear a considerable resemblance to the responses to above-normal SST conditions in the IWP sector in the summer following the peak phase of warm ENSO events, as obtained by L05 (see their Fig. 10) using an entirely different GCM at GFDL.[5] The spatial relationships between various meteorological fields are similar to those associated with extended heat waves and droughts observed over the United States, as documented by Chang and Wallace (1987) and others.

Model experiments under various global warming scenarios have projected increased drying over continental interiors during the summer season (e.g., Gregory et al. 1997; Wetherald and Manabe 1999). The results in Fig. 9 suggest that tropical oceanic warming, especially in the IWP sector, may be a contributing factor to meteorological conditions that are conducive to summer dryness over certain land regions, such as North America.

8. Summary and discussion

In the present study, we began by contrasting the composite patterns for El Niño and La Niña episodes occurring in the first two decades of the 1951–2000 or 2001–50 periods against those for the last two decades of the same periods (Figs. 2 and 3). This analysis reveals that the strength of anomalies over North America during La Niña events increases progressively with time; whereas the anomalies in El Niño episodes gradually decline in intensity. Much of the diagnostics in the succeeding sections are aimed at identifying the mechanisms contributing to such secular changes. We first demonstrated that the current generation of climate models at GFDL is capable of reproducing the essential characteristics of the observed interannual anomalies over North America associated with the mature phase of El Niño and La Niña events in the boreal cold season (Figs. 4 and 5). These ENSO-related signals exhibit a notable degree of commonality across different climatic settings, as incorporated in the C20C and A1B experiments. We then examined the effects of the secular SST warming trends in the IWP sector, as reproduced in the C20C experiment for 1951–2000 and as projected by the A1B experiment in 2001–50 (Fig. 1). The atmospheric response patterns in the North Pacific–North American region to this IWP forcing (Fig. 6) are positively correlated with the anomalies occurring in La Niña, and negatively correlated with those associated with El Niño. The response of the North American climate and the zonally averaged circulation to the joint presence of ENSO and IWP forcings (Figs. 7 and 8) is approximately equal to the linear sum of the responses to these two forcings individually. Reinforcements (cancellations) between the effects of IWP warming and La Niña (El Niño) lead to higher amplitudes of the combined responses as simulated in the T(IWP)+LN runs as compared to those in the T(IWP)+EN runs. Such interactions between the signals linked individually to IWP and ENSO forcings offer a partial explanation for the long-term increase (decrease) in strength of atmospheric anomalies in La Niña (El Niño). In the warm season, the response in North America to IWP warming (Fig. 9) is stronger than that to ENSO forcing, and is characterized by a prominent warm and dry anomaly over much of the continental United States. The accompanying patterns of the surface wind and upper-level geopotential height over the interior of the North American landmass are reminiscent of the meteorological features related to prolonged droughts and heat spells in that region. The impacts of IWP warming on the North American climate throughout the year have implications on the relative frequency and intensity of severe precipitation and temperature anomalies in that region during La Niña and El Niño events.

A parallel suite of sensitivity runs [i.e., EN, LN, T(IWP), T(IWP)+EN, and T(IWP)+LN] have also

[5] Note that the SST anomalies in L05 were generated by the atmospheric bridge mechanism linking ENSO forcing in the tropical central and eastern Pacific to interannual oceanic variability in the IWP region (see Klein et al. 1999; Alexander et al. 2004); whereas the IWP forcing in the present work is associated with long-term climatic trends related to natural and anthropogenic causes.

been conducted with *observed* SST forcings derived from composites over the nine El Niño and nine La Niña events in the 1951–2000 period (see lists in section 3), and the SST trend in the IWP region that has occurred in that 50-yr period. The output from these additional runs has been subjected to the same diagnoses as those performed on the corresponding runs based on *simulated* SST forcings from the C20C and A1B experiment, as described in the previous sections. The results (not shown for the sake of brevity) are in support of the key findings of this study. In particular, the response of the model atmosphere to IWP warming is positively (negatively) correlated with the La Niña (El Niño) response in the North Pacific–North American sector, and the net response to combined IWP and ENSO forcings can be approximated as the linear sum of these two individual effects.

Among the various ocean sites with notable long-term SST trends, we have been concerned exclusively with the secular warming in the IWP sector. Inspection of the patterns in Fig. 1 indicates that the deep tropical eastern-central Pacific (DTEP) region also exhibits spatially coherent rising SST trends in both 1951–2000 and 2001–50. The climatic impacts of the SST warming in the latter region have been explored by sensitivity runs analogous to T(IWP), except that the 50-yr increase in the DTEP region (15°S–15°N, 160°E to the South American coast) has been inserted in the lower boundary condition. Such additional runs [hereafter referred as T(DTEP)] have been conducted on the basis of SST forcings from observations of the 1951–2000 period (see Fig. 1a). The responses of the North American and zonally averaged climates to the SST trend in DTEP, as deduced from the patterns of T(DTEP) (not shown), bear some resemblance to, but are considerably weaker than, the corresponding El Niño responses, as inferred from the patterns of EN (not shown) based on the composite SST forcing for the nine observed warm events. The relatively smaller amplitudes of the signals generated in T(DTEP) may be attributed to the weaker SST forcing due to the long-term trend (at most 1°C increase in 50 yr, see Fig. 1a) as compared to the composite strength of the observed SST anomalies in the DTEP during El Niño events (about +2°C, see L05). The emphasis in this study on the results from the T(IWP), EN, and LN runs is predicated upon the stronger responses in these integrations than those in T(DTEP). It might be of interest to perform further evaluations of the influences of the secular SST changes in other maritime region (particularly the North Pacific and the Atlantic) by changing the forcing domain in model runs analogous to T(IWP) and T(DTEP). By the same token, the relative importance of the SST trend in different sites within IWP (in particular, the Indian Ocean versus the western Pacific) could be assessed more thoroughly by conducting separate sensitivity runs based on SST forcing prescribed in each of these subregions. The results from such investigations on the atmospheric responses to the SST changes at various sites in the World Ocean, as well as the linearity of the responses to combinations of forcing at these sites, could be compared with the findings based on the more systematic approach adopted by Barsugli and Sardeshmukh (2002) and Barsugli et al. (2006). These authors considered a large array of SST anomaly "patches," and computed the model responses to each of these patches. SST sites to which target fields of interest are particularly sensitive could then be identified by linearly combining the responses to the individual patches.

The secular changes in the background state of the SST pattern in the tropical Pacific, as alluded to in the preceding paragraph, could conceivably alter the characteristics (such as amplitude and frequency of occurrence) of ENSO variability, which could in turn affect North American climate. These issues have recently been explored by several studies using output from the ensemble of coupled models contributing to the IPCC effort. Van Oldenborgh et al. (2005) reported that the six most realistic models project no significant change in ENSO amplitudes in the future, and concluded that global warming exerts little influence on ENSO behavior. Guilyardi (2006) noted a considerable spread of El Niño behavior among a similar subset of realistic models, with no noticeable change in El Niño frequency and a slight indication of increased El Niño amplitude in a warmer climate. Merryfield (2006) also found a wide scatter of changes in ENSO properties among the IPCC model projections, with no clear consensus on amplitude, and a small mean decrease in the ENSO period. More investigations are evidently needed to delineate the effects of global climate change on ENSO variability, and the potential link between IWP warming and ENSO behavior.

Much of the analysis in the present work has been devoted to the effects of IWP warming and ENSO on the climate in the North American sector. It has been well recognized that ENSO influences are not confined to that region, but extend to many other sites throughout the globe. By virtue of the strong zonal symmetry of the responses to SST forcing in IWP, the warming trend in that site also has impacts across a broad range of longitudes. Further study is needed to delineate the modulation by IWP warming of ENSO responses in various geographical locations beyond the North American domain.

The methodology of this study hinges on the prescription of SST conditions at various locations of interest, and the simulation of the responses to these imposed forcings in sensitivity runs using an atmospheric GCM. This approach is effective in identifying the atmospheric signals associated with specific SST anomalies, and in diagnosing the interplay between atmospheric patterns in response to different types of SST forcing. However, these sensitivity runs are only suited for delineating the effects of the ocean on the atmosphere; they do not address other complementary issues of the coupled problem, such as the origin of the SST forcings themselves, and the feedbacks of the atmospheric responses on the ocean. The limitations of atmospheric GCM experiments subjected to prescribed SST forcing for understanding regional climate changes have been noted by Douville (2005) and Copsey et al. (2006), among others. Furthermore, insertion of SST anomalies in the IWP region leads to SST gradients near the boundary of this domain (see the green borders in Figs. 1a,b). Such artificial features might contribute to the response as simulated in the model atmosphere. The findings reported here should therefore be interpreted with all of the above issues in mind.

In the present study, we have focused on the interactions between atmospheric responses to ENSO and to long-term changes in the climate system, as expressed in the warming of the IWP sector. It should be noted that the modified SST conditions in IWP and other parts of the World Ocean represent only one facet of the anticipated global climate change in the coming decades. Other perturbations of the climate system (such as increased land surface temperatures, especially in high latitudes; alterations of the atmospheric and oceanic basic states; etc.) could also play significant roles in modulating the ENSO signals. These additional factors, as well as the attendant feedback processes, need to be taken into account in a more comprehensive assessment of ENSO-related variability under various climate change scenarios.

The SST anomalies related to IWP warming and ENSO, as used in forcing the sensitivity runs, have been derived from output of the C20C and A1B experiment based on coupled GCMs. Much progress has been made toward our understanding of the nature of SST anomalies associated with ENSO (e.g., see reviews by Philander 1990; Wang and Picaut 2004). On the other hand, our knowledge of the processes contributing to the secular warming in the IWP sector remains rather limited. More in-depth investigations are needed to clarify the relative roles of flux exchanges across the air–sea interface and internal ocean dynamics in causing the long-term SST increase in that region. Such analyses should benefit from the availability of model data generated by coupled GCMs, as conducted at GFDL and other research centers based on various appropriate forcing scenarios.

Acknowledgments. We would like to thank Isaac Held, John Lanzante, Gabriel Vecchi, and the official reviewers for offering insightful comments on the preliminary draft of this manuscript. Their input was very helpful in improving the clarity of the presentation of our findings.

REFERENCES

Alexander, M. A., N.-C. Lau, and J. D. Scott, 2004: Broadening the atmospheric bridge paradigm: ENSO teleconnections to the tropical West Pacific-Indian Oceans over the seasonal cycle and to the North Pacific in summer. *Earth's Climate: The Ocean–Atmosphere Interactions, Geophys. Monogr.,* Vol. 147, Amer. Geophys. Union, 85–103.

Barsugli, J. J., and P. D. Sardeshmukh, 2002: Global atmospheric sensitivity to tropical SST anomalies throughout the Indo-Pacific basin. *J. Climate,* **15,** 3427–3442.

——, S.-I. Shin, and P. D. Sardeshmukh, 2006: Sensitivity of global warming to the pattern of tropical ocean warming. *Climate Dyn.,* **27,** 483–492.

Chang, F.-C., and J. M. Wallace, 1987: Meteorological conditions during heat waves and droughts in the United States Great Plains. *Mon. Wea. Rev.,* **115,** 1253–1269.

Copsey, D., R. Sutton, and J. R. Knight, 2006: Recent trends in sea level pressure in the Indian Ocean region. *Geophys. Res. Lett.,* **33,** L19712, doi:10.1029/2006GL027175.

Delworth, T. L., and Coauthors, 2006: GFDL's CM2 global coupled climate models. Part I: Formulation and simulation characteristics. *J. Climate,* **19,** 643–674.

Douville, H., 2005: Limitations of time-slice experiments for predicting regional climate change over South Asia. *Climate Dyn.,* **24,** 373–391.

Gregory, J. M., J. F. B. Mitchell, and A. J. Brady, 1997: Summer drought in Northern midlatitudes in a time-dependent CO_2 climate experiment. *J. Climate,* **10,** 662–686.

Guilyardi, E., 2006: El Niño-mean state-seasonal cycle interactions in a multi-model ensemble. *Climate Dyn.,* **26,** 329–348.

Halpert, M. S., and C. F. Ropelewski, 1992: Surface temperature patterns associated with the Southern Oscillation. *J. Climate,* **5,** 577–593.

Hoerling, M. P., and A. Kumar, 2003: The perfect ocean for drought. *Science,* **299,** 691–694.

——, ——, and M. Zhong, 1997: El Niño, La Niña, and the nonlinearity of their teleconnections. *J. Climate,* **10,** 1769–1786.

——, ——, and T. Xu, 2001: Robustness of the nonlinear climate response to ENSO's extreme phases. *J. Climate,* **14,** 1277–1293.

Kalnay, E., and Coauthors, 1996: The NCEP/NCAR 40-Year Reanalysis Project. *Bull. Amer. Meteor. Soc.,* **77,** 437–471.

Kaplan, A., M. A. Cane, Y. Kushnir, A. C. Clement, M. B. Blumenthal, and B. Rajagopalan, 1998: Analyses of global sea surface temperature 1856-1991. *J. Geophys. Res.,* **103** (C9), 18 567–18 590.

Kattsov, V. M., and P. V. Sporyshev, 2006: Timing of global

warming in IPCC AR4 AOGCM simulations. *Geophys. Res. Lett.,* **33,** L23707, doi:10.1029/2006GL027476.

Klein, S. A., B. J. Soden, and N.-C. Lau, 1999: Remote sea surface temperature variations during ENSO: Evidence for a tropical atmospheric bridge. *J. Climate,* **12,** 917–932.

Knutson, T. R., and Coauthors, 2006: Assessment of twentieth-century regional surface temperature trends using the GFDL CM2 coupled models. *J. Climate,* **19,** 1624–1651.

Kumar, A., and M. P. Hoerling, 2003: The nature and causes for the delayed atmospheric response to El Niño. *J. Climate,* **16,** 1391–1403.

——, A. Wang, M. P. Hoerling, A. Leetmaa, and M. Ji, 2001: The sustained North American warming of 1997 and 1998. *J. Climate,* **14,** 345–353.

Lau, N.-C., A. Leetmaa, M. J. Nath, and H.-L. Wang, 2005: Influences of ENSO-induced Indo-Western Pacific SST anomalies on extratropical atmospheric variability during the boreal summer. *J. Climate,* **18,** 2922–2942.

——, ——, and ——, 2006: Attribution of atmospheric variations in the 1997–2003 period to SST anomalies in the Pacific and Indian Ocean basins. *J. Climate,* **19,** 3607–3628.

Lin, S.-J., 2004: A "vertically Lagrangian" finite-volume dynamical core for global models. *Mon. Wea. Rev.,* **132,** 2293–2307.

Merryfield, W. J., 2006: Changes to ENSO under CO_2 doubling in a multimodel ensemble. *J. Climate,* **19,** 4009–4027.

Mitchell, T. D., and P. D. Jones, 2005: An improved method of constructing a database of monthly climate observations and associated high-resolution grids. *Int. J. Climatol.,* **25,** 693–712.

Nakićenović, N. J., and Coauthors, 2000: *IPCC Special Report on Emission Scenarios*. Cambridge University Press, 599 pp.

Nigam, S., 2003: Teleconnections. *Encyclopedia of Atmospheric Sciences,* J. R. Holton, J. A. Curry, and J. A. Pyle, Eds., Vol. 6, Academic Press, 2243–2269.

Philander, S. G. H., 1990: *El Niño, La Niña, and the Southern Oscillation*. Academic Press, 289 pp.

Rasmusson, E. M., and T. H. Carpenter, 1982: Variations in tropical sea surface temperature and surface wind fields associated with the Southern Oscillation/El Niño. *Mon. Wea. Rev.,* **110,** 354–384.

Ropelewski, C. F., and M. S. Halpert, 1986: North American precipitation and temperature patterns associated with the El Niño-Southern Oscillation (ENSO). *Mon. Wea. Rev.,* **114,** 2352–2362.

——, and ——, 1987: Global and regional scale precipitation patterns associated with the El Niño/Southern Oscillation. *Mon. Wea. Rev.,* **115,** 1606–1626.

——, and ——, 1989: Precipitation patterns associated with the high index phase of the Southern Oscillation. *J. Climate,* **2,** 268–284.

Seager, R., N. Harnik, Y. Kushnir, W. Robinson, and J. Miller, 2003: Mechanisms of hemispherically symmetric climate variability. *J. Climate,* **16,** 2960–2978.

Smith, T. M., and R. W. Reynolds, 2004: Improved extended reconstruction of SST (1854–1997). *J. Climate,* **17,** 2466–2477.

Trenberth, K. E., G. W. Branstator, D. Karoly, A. Kumar, N.-C. Lau, and C. Ropelewski, 1998: Progress during TOGA in understanding and modeling global teleconnections associated with tropical sea surface temperatures. *J. Geophys. Res.,* **103** (C7), 14 291–14 324.

van Oldenborgh, G. J., S. Y. Philip, and M. Collins, 2005: El Niño in a changing climate: A multi-model study. *Ocean Sci.,* **1,** 81–95.

Vecchi, G. A., and B. J. Soden, 2007: Global warming and the weakening of the tropical circulation. *J. Climate,* **20,** 4316–4340.

Wang, C., and J. Picaut, 2004: Understanding ENSO physics—A review. *Earth's Climate: The Ocean–Atmosphere Interactions, Geophys. Monogr.,* Vol. 147, Amer. Geophys. Union, 21–48.

Wetherald, R. T., and S. Manabe, 1999: Detectability of summer dryness caused by greenhouse warming. *Climatic Change,* **43,** 495–511.

Wittenberg, A. T., A. Rosati, N.-C. Lau, and J. J. Ploshay, 2006: GFDL's CM2 global coupled climate models. Part III: Tropical Pacific climate and ENSO. *J. Climate,* **19,** 698–722.